A RUGGED FIBER OPTICS MONITORING SYSTEM FOR HELICOPTER ROTOR BLADES

Bottasso Luigi M., luigi.bottasso@leonardocompany.com, Leonardo Helicopters (Italy)
Sala Giuseppe, giuseppe.sala@polimi.it, Politecnico di Milano (Italy)
Bettini Paolo, paolo.bettini@polimi.it, Politecnico di Milano (Italy)
Tagliabue Paolo, paolo.tagliabue@opticalsensing.it, Optical Sensing Technologies (Italy)
Corbani Franco, franco.corbani@opticalsensing.it, Optical Sensing Technologies (Italy
Platini Emilio, emilio.platini@leonardocompany.com, Leonardo Helicopters (Italy)
Guerra Andrea, andrea.guerra@leonardocompany.com, Leonardo Helicopters (Italy)
Anelli Andrea, andrea.anelli@leonardocompany.com, Leonardo Helicopters (Italy)

Abstract
Health and Usage Monitoring (HUM) and Structural Health Monitoring (SHM) technologies play an increasingly important role in aerospace applications, for example in support to fleet maintenance and for test and development purposes. We describe the design, manufacture and integration of an advanced blade strain monitoring system for the tail rotor of the AW139 helicopter. The goal was two-fold: to demonstrate the feasibility of a rugged rotor-based interrogation system and the practical embedding of Fiber Bragg Gratings (FBG) sensors within composite rotor blades. This task required careful study of the optimal fiber path within the constraints of the blade composite structure and the ply stacking sequence. A temperature compensation method was developed to decouple thermal strain. An integrated interrogation-communication system housed in a dedicated beanie was developed with the capability to withstand the harsh high-g environment of a rotor hub. In order to avoid the need for slip rings for power and data transfer between fixed and rotating frames, the interrogator was designed as a self-contained unit equipped with batteries and wireless data transmission capability. This rugged monitoring system offers cleaner aerodynamics and longer sensor life compared to traditional strain gauges and represents a stepping stone towards the development of future fiber-based HUM with photonics chip interrogators.

1. INTRODUCTION

As a premise of the initiative here described we observe that the time appears ripe for a fruitful collaboration among the research community and rotorcraft manufacturers who share an interest in optronics technologies for Health and Usage Monitoring (HUM) aplications.

We note a recent surge both in investment and in technological spin-offs in the field, a trend which will likely continue to benefit the aerospace sector. We believe that optronics-based HUM technology will have an increasing impact on the industry in the years ahead.

Fiber Bragg Grating (FBG) sensors have long been used for strain and pressure measurements in various fields[1 2]. The minimally invasive form of the fiber, combined with its reliability and intrinsic resistance to harsh environments, represent attractive features. Furthermore, the possibility of frequency or time[3] multiplexing allows for distributed sensing along the same optical path, thus with fewer cables than traditional strain gauges.

On the downside, the typical fiber readout apparatus (the FBG interrogator) presents some disadvantages. These systems tend to be bulky, fragile and expensive, factors which have severely limited the diffusion of FBG sensing technology in certain industrial domains; this explains the currently marginal adoption in aerospace structural health monitoring.

Aerospace applications dictate compact, reliable and ruggedized FBG interrogators for use in demanding operational scenarios such as on a helicopter rotor blade. If these requirements could be met, there would be room for a more widespread use of FBG sensors for in-situ structural monitoring on both rotary and fixed wing platforms.

The origins of the present work can be traced back to the quest for an improved rotor load survey system. Load surveys are performed on helicopter prototypes during development test flights. Here, helicopters are instrumented with strain gauges bonded in various structural locations to monitor loads across the whole flight envelope.

Data are recorded on board or streamed to a ground station via telemetry for subsequent analysis and comparison with predicted design loads.

Figure 1: The AW139 twin engine helicopter

The tail rotor blades, which represent one of the most critical monitoring areas, were selected for the case study here described.

Figures 1 and 2 show the AW139 medium twin-engine helicopter and a close-up of its tail rotor hub; this rotorcraft model was used as the reference platform for the work.

Figure 2: Close-up on the hub of the AW139 helicopter tail rotor

A fiber sensor system suitable for a tail rotor application shall have a readout unit meeting strict weight, size, power and ruggedness requirements, while at the same time ensuring remote interrogation of several FBG sensors with high precision and speed.

A custom-designed interrogator was thus specifically conceived and developed for the purpose, packaged into a compact portable module. We believe this represents a step forward in integration compared to the state of the art.

The benefits of the FBG technology can be better appreciated by looking at some shortcomings of the standard solution based on electrical resistance strain gauges.

Rainy weather conditions typically preclude or limit the ability to conduct helicopter flight tests with instrumented rotor blades due to the erosive effect produced by high-speed water droplets on traditional strain gauges. Additionally, the drag produced by non-flush sensors protruding outside the airfoil reduces the maximum operational flight speed by several knots.

A practical advantage provided by the fiber technology lies in its capability to be encapsulated within a structure, in particular a composite material laminate; this condition ensures protection from external agents as well as a flush surface finish and thus lower drag.

This is a case where the right technological choice translates directly into measurable operational benefits.

2. INTERROGATOR DESIGN

The interrogator was designed around a set of requirements derived from the specific application on a rotor; they are captured in the following list:

- Max/min strain at blade root: +4000/-1000 $\mu\epsilon$
- Rotational speed: 1464 RPM (102% of nominal)
- Centrifugal acceleration: 432 g @ 18 cm from axis
- Vibration-induced accelerations: max 10 g (x, y, z)
- Data transfer from rotor to fixed frame: wireless
- Sampling rate: 1024 Hz
- Power source: battery (life $\geq$ 1 h)

The interrogator is housed in a beanie cap bolted to the "spider", a cross-shaped element connecting the blade pitch links to a coaxial actuator rod; the layout is illustrated in Figure 3.

Optical fiber linkage between the beanie and the articulated blades is ensured through flexible cable connectors (not illustrated) with quick link/disconnect capability, which accommodate blade flapping, lead lag and pitch variation.

2.1. System Architecture Overview

Scope of this section is the brief description of some of the key system design features including: the sensor layout, the optoelectronic ”core”, the broadband optical source and its driving electronics, the signal

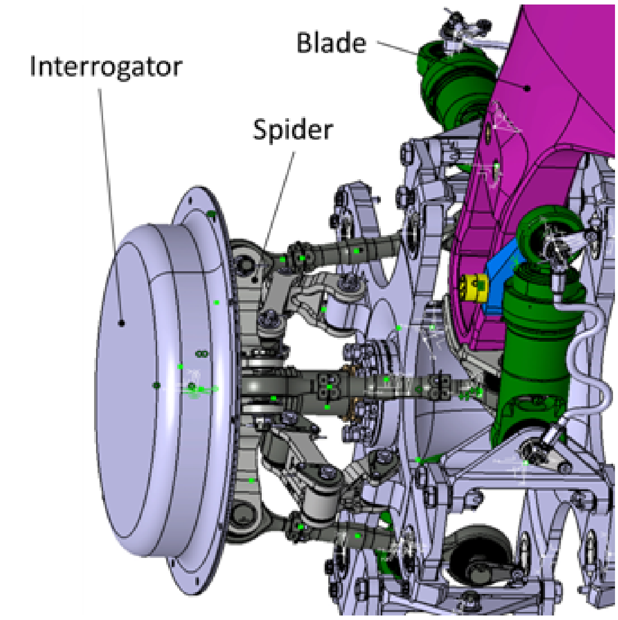

Figure 3: 3D model of the tail rotor hub and beanie assembly

conditioning and the mechanical and structural integration.

The sensor layout was designed to acquire all relevant loads acting on a tail rotor blade during operation: axial, in-plane / out-of-plane bending and torsion in the blade body, plus the axial load in the blade handle. Furthermore, temperature was measured in selected locations for sensor calibration purposes.

The AW139 tail rotor has four blades, all subjected to the same cyclic load conditions, thus in principle one monitored blade could suffice. However, the chosen layout includes two opposite blades provided with sensors and two standard blades without sensors. It was decided to acquire half of the load components on one blade and the remaining half on the second blade to complete the desired data set. The rationale for the choice was to reduce sensor installation complexity on any individual blade.

Each of the monitored blades has four fibers each carrying 2 FBG sensors, for a total of eight fibers and sixteen sensors. The complete interrogator system consists of four identical units each capable of handling two fibers, thus four FBGs.

The Bragg wavelengths of the FBG sensor pair on each fiber are the same for all fibers; the interrogators are thus optimized to read wavelengths in the two selected spectral regions of the FBG sensors. This configuration choice makes the system simpler and more robust because the interrogators and the fibers are interchangeable.

The selected wavelengths for the FBG sensors are 1538.5 nm and 1548.5 nm in a nominal, unloaded condition. The reason for the choice of the selected wavelength pair lies in the emission characteristics of the optical source and in the need to ensure adequate spectral separation.

In absence of suitable off-the-shelf equipment, the interrogator had to be designed essentially from scratch. The general system layout and associated block diagram for an interrogator module is illustrated in Figure 4.

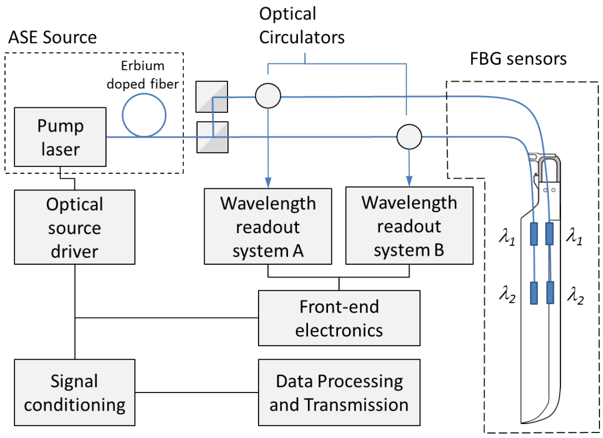

Figure 4: Block scheme of one interrogator module reading two fibers in a frequency-modulation arrangement

The search for a suitable optical source which could offer thermal stability, a flat emission spectrum and uncooled operation, led to the choice of an Erbium-Doped Fiber Laser (EDFL) ASE (Amplified Spontaneous Emission) source, pumped with an uncooled pigtailed laser diode. EDFL's advantages include high beam quality, broad tunable wavelength and small size[4].

During preliminary bench test a SLED (Superluminescent Light Emitting Diode) was used. A SLED is an edge-emitting semiconductor light source which combines the high power and brightness of laser diodes with the low coherence of conventional light-emitting diodes.

In our case a single ASE source was used to interrogate two fibers simultaneously (and thus four FBGs) through a dual-channel setup (see Figure 4).

The general principle used for FBG interrogation is based on filtering the signal reflected back from the FBGs, it is therefore a filter-based readout system. The overall scheme is illustrated in Figure 5.

The signal is sent through a beam-splitter, each branch is subsequently filtered with a separate band-pass filter to select the reflection from one or the other of the sensor pair.

Subsequently each signal is split again and sent through discriminator filters, essentially two linear transmittance filters (LTF) with opposite slopes, then to the photodiodes. In order to enhance the sensitivity and to make the system tolerant to optical power variations the signal is normalized after measurement.

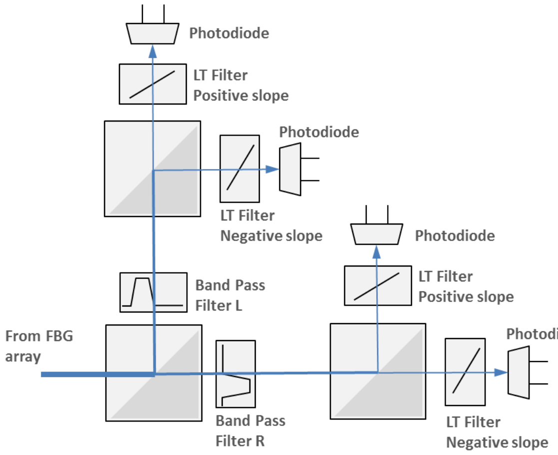

Figure 5: Scheme of a filter-based wavelength read-out system

The opposite slope discriminators are obtained by using the rising and falling edges of bell-shaped filters. The FBG sensors operating range is in the cross-over region of these filters.

To achieve better ruggedness, compact design and ease of integration, the actual optical hardware used in the interrogator is based on fiber-optics components, as shown in Figure 6. Here, the cube reflectors and band-pass filters are replaced by much smaller fiber optic filters and splitters.

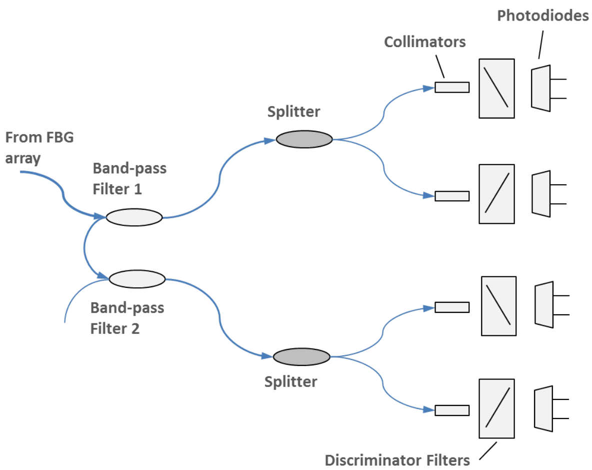

Figure 6: Scheme of the fiber-based splitting network

A benefit of using a mix of fiber-based and micro-optics components consists in the ability to optimize the system layout both in terms of size and optical power budget. Moreover this ensures robustness and compactness of the assembly.

The optical signals coming from the sensors are directed to the filters-photodiodes by means of a battery of optical collimators, each of which had to be carefully aligned to its filter because the spectral response of the discriminator may be affected by misalignment errors.

The module was therefore installed with the help of a tunable laser. The nominal filter transfer function is in fact known, and a laser scanning over the operating wavelength range of each filter allows double checking of the correct alignment across collimator, filter and photodiode.

Once aligned and once the signal levels and gain have been regulated, the average system sensitivity is around 1.29 V/nm on every channel.

The reduced volume available on the rotor hub, the high centrifugal accelerations and the vibration levels were among the most demanding design constraints. As a consequence, each of the four interrogation units was encapsulated within a custom-designed plastic enclosure manufactured through 3D printing, incorporating receptacles for the confinement of optical components and fiber organizers.

Each interrogator unit has a layered structure with modules stacked together; each layer houses different functions. The bottom layer contains the optical source, the main interrogation module and a first fiber organizer. The middle layer houses a second fiber organizer with the components necessary to handle and process the optical signals to and from the FBGs. The top layer contains the battery pack, power supply electronics and a radio-board with micro-controller to perform the AD conversion of the analog signals generated by the system and to send them to a receiving station through ZigBee wireless connection. See Figures 7 and 8.

Table 1 summarizes the interrogator system specifications.

Figures 9 and 10 show the four units assembled on the beanie back plate during static test. In the first picture the central position is occupied by a wireless node which was used during preliminary tests, this was later substituted by ZigBee radio modules integrated inside each unit box. The central position was then occupied by a switch as shown in Figure 10.

2.2. Beanie structural design

The beanie is composed of a back plate made of carbon fiber composite and a fiberglass cover, the

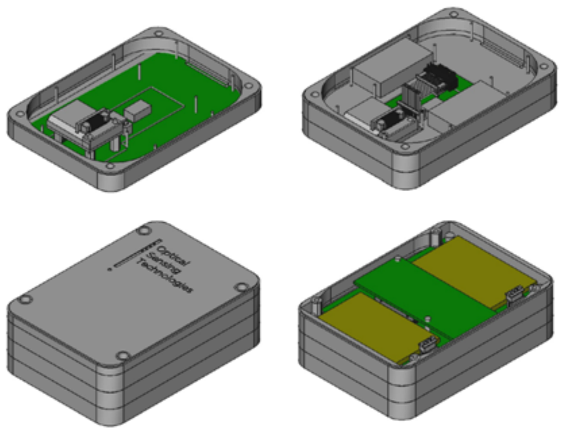

Figure 7: Interrogator unit internal structure, clockwise from top left; layer 1: ASE source and main interrogation module; layer 2: optical components for readout of two fibers; layer 3: battery pack with ZigBee module and electronics board, cover plate

Table 1: Interrogator system specifications

Size	120x85x40 mm
Weight	308 g incl. battery pack
Power supply	5 V, 2xLiPo batteries in series, 3.7 V, 1300 mAh each
Current usage and Voltage drop	100 mA per unit, 200 mV/h drop in continuous operation
Performance @1kHz, 12 bit ADC	Sensitivity: variable (1.29 V/nm min)
	Resolution: 15 pm
WL range	2.3 nm (measured), 4 nm (max range per sensor)

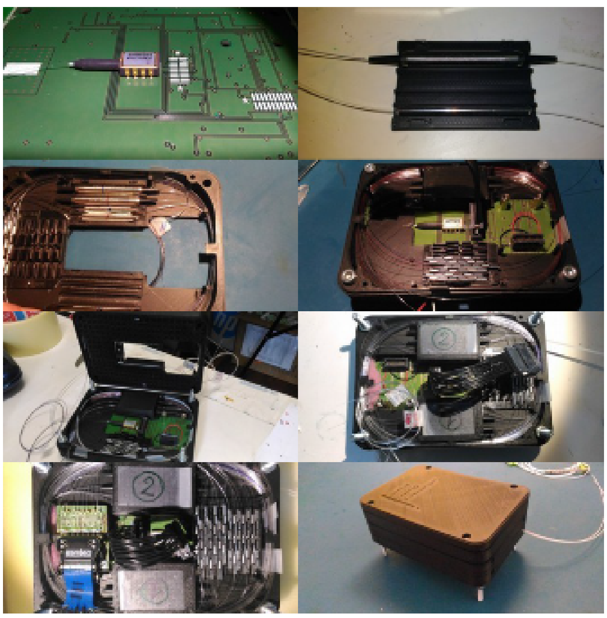

Figure 8: Assembly phases for the interrogator unit

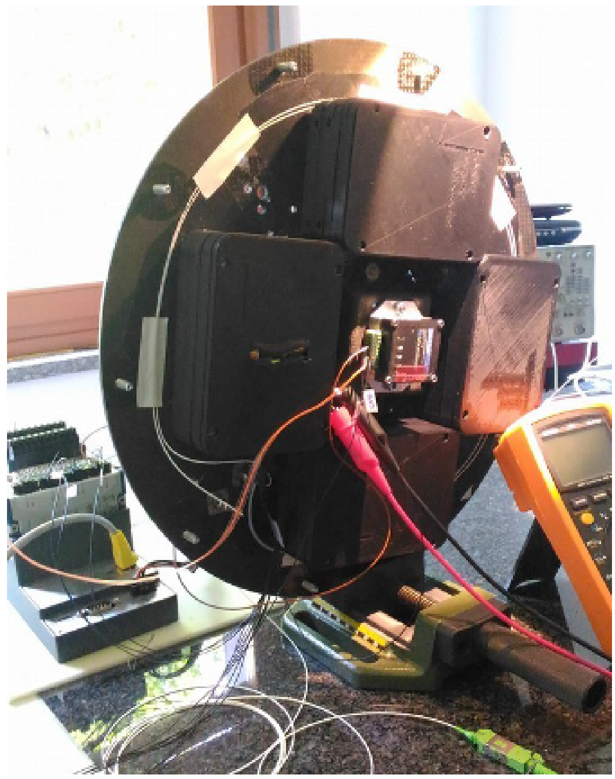

Figure 9: The beanie with the open cover, showing the four interrogator units

latter being transparent to radio frequencies as required by wireless operation.

The four interrogators were bolted to the plate in a radially symmetrical layout for obvious balancing requirements, with the center position being used for a power on/off switch, see Figure 10.

Finite element analyses were performed to evaluate operational stresses and deformations under load, Figures 11 and 12 show displacement plots of the cap and plate portions. The four interrogator modules were modelled with lumped masses of 320 g each, linked through multi-point constraints to the four connection points.

The maximum deflections computed in the NASTRAN analyses were well within the acceptable limits.

2.3. Spin rig qualification test

The optoelectronic components used in FBG interrogators comply with certification requirements mainly tailored to applications in the telecommunications industry. There, the typical qualification test criteria require high-g shock resistance of components.

However, sustained exposure to vibration and

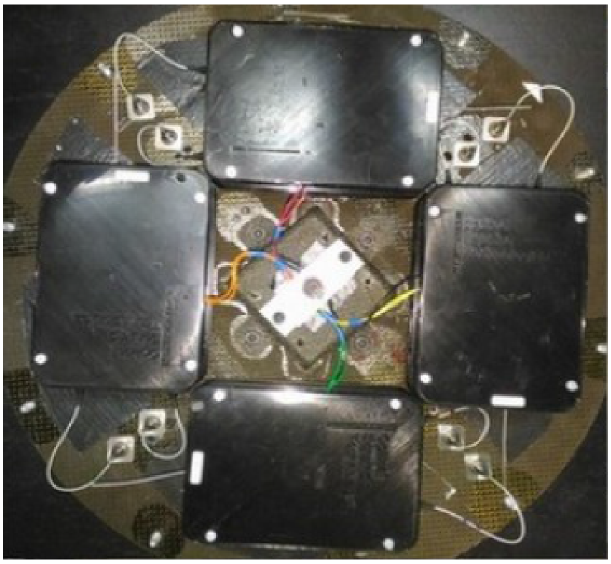

Figure 10: The beanie with the open cover, showing the four interrogator units and the central switch

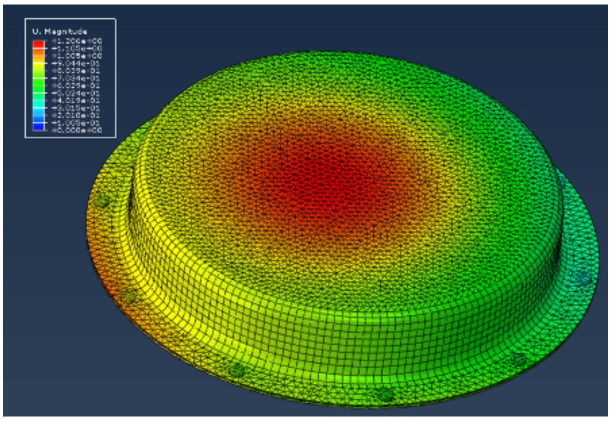

Figure 11: Beanie FEM - top cover

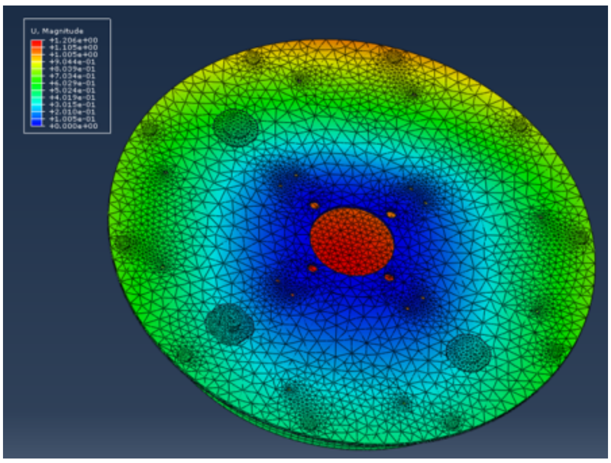

Figure 12: Beanie FEM - back plate

high-g field is not a realistic loading condition in telecommunications. Therefore it was necessary to qualify the components through dedicated test setups.

A total of eight different test runs were performed on a spin-rig. Each run was aimed at a specific test configuration, starting from the level of individual components up to the complete interrogator module. The optoelectronic components, housed inside a beanie with battery power packs and wireless nodes, were spun up to 1600 rpm to simulate operational loads and vibrations. Real time wireless monitoring was performed to check any significant detrimental effects on performance.

Figure 13 illustrates a rear view of the beanie back plate installed on the spin rig.

All tests were successfully completed with nominal performance of the equipment.

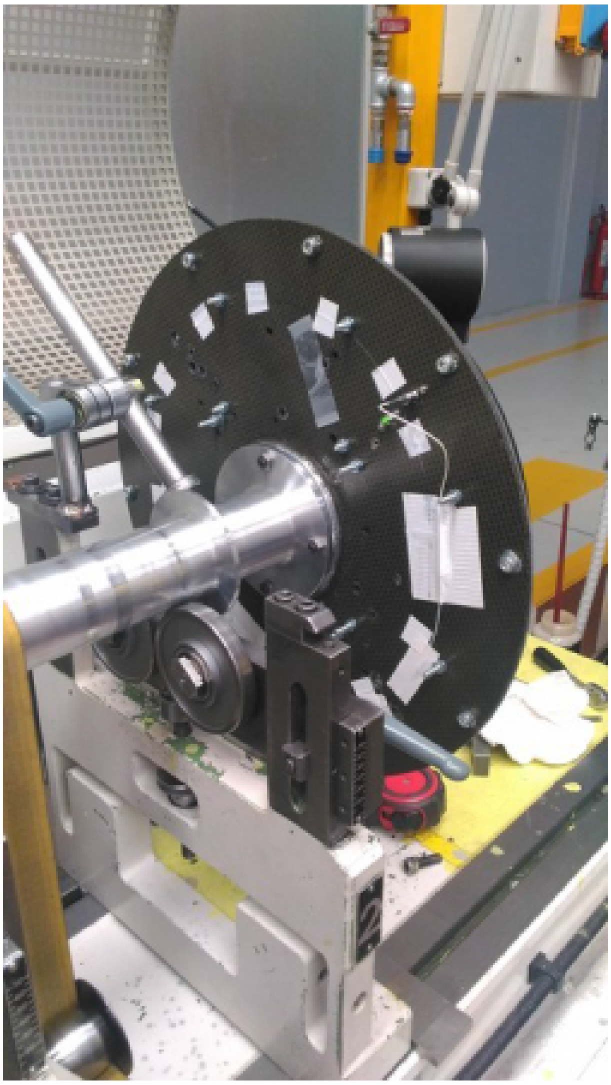

Figure 13: The beanie instrumented for test at the spin rig

3. FBG EMBEDDING WITHIN BLADES

3.1. Blade design

Figure 14 is a section of a tail rotor blade resting on its upper airfoil surface, showing the internal structure. This includes a spar made of unidirectional fiberglass which is then wrapped with bidirectional plies and internally filled with foam. The trailing edge portion is made of Nomex honeycomb and the blade is then covered with an external skin shell made of $\pm 45^\circ$ plies and completed with an erosion shield for leading edge protection.

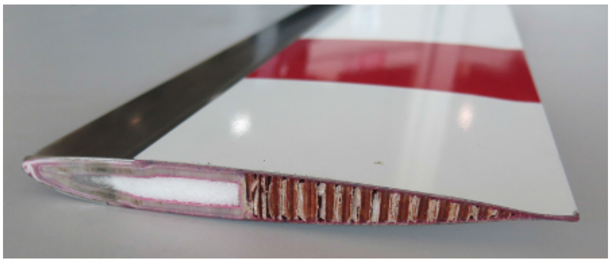

Figure 14: Tail rotor blade section, showing the internal spar structure

3.2. Blade production cycle

The tail rotor blade comprises several distinct structural parts. The spar is the D-shaped component designed to carry most of the axial, bending and torsional loads. It occupies roughly the front 40% of the blade chord and represents most of the blade section mass. Its position effectively moves the center of gravity forward, close to the pitch hinge axis, thus helping reduce the control torque.

The spar is built with unidirectional (UD) straps running along the longitudinal blade direction to carry the large axial load; the straps are then wrapped with $\pm 45^\circ$ plies to create a torsion box.

Honeycomb filler material placed behind the spar gives the desired aerodynamic shape to the airfoil with minimal weight penalty.

The blade skin consists of further composite material layers with fibers oriented at $\pm 45^\circ$ wrapping all together in an external shell which guarantees a good aerodynamic finish.

The trailing edge is obtained by gluing the upper and lower skins together. The leading edge erosion shield covers the front part of the airfoil with a nickel alloy sheet.

The blade production involves three separate polymerization steps which are briefly described.

Spar manufacturing starts with an automated fiber deposition process to generate the longitudinal straps for the blade handle regions which then merge into the spar. In this phase, both upper and lower straps are created in a single piece which are successively separated in two equal parts, then impregnated with resin and placed in the mold for curing. Subsequently, the handle is assembled by installing the blade root support block and an inner handle ring interposed between the upper and lower straps. The U-shaped handle region is then manually wrapped with $\pm 45^\circ$ plies to create a torsion box.

The manufacturing of the spar torsion box follows, with the aim of providing torsional resistance to the spar. This process consists in the manual deposition of $\pm 45^\circ$ plies wrapping the strap assembly; a second polymerization cycle follows.

Then comes the gluing of the honeycomb filler to the spar, where the honeycomb is machined to the required airfoil shape. The fragile Nomex material has to be stabilized before machining; this is done through the injection of water-soluble foams.

The external skin, constituted by plies with $\pm 45^\circ$ fiber orientation, is applied to the assembly which then undergoes the third and final curing step.

The nickel erosion shield is finally glued in a recess obtained on the blade leading edge, to ensure a smooth surface. Figure 15 illustrates the blade in two stages: handle assembly and finished product; these allow visualization of some key components and structural elements.

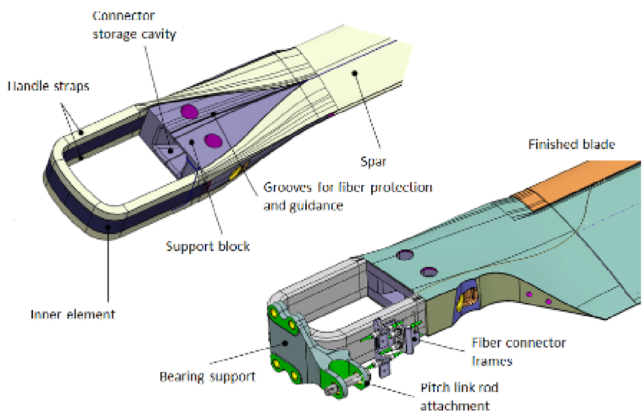

Figure 15: The blade in two production stages with its main components

3.3. Design of the blade sensor system

Each fiber has two FBG sensors with different wavelengths, the same for all fibers. The wavelengths were chosen to allow the interrogator to easily distinguish the signal coming from the two sensors on a same fiber. The selected wavelength pair for the

FBG sensors is 1538.5 and 1548.5 nm in a nominal, unloaded condition.

Table 2 summarizes the sensors and fibers, describing the role of each fiber in the blade load assessment. For simplicity, the two sensor wavelengths are mentioned as R and B (for red and blue, referring to the longer and shorter wavelengths respectively).

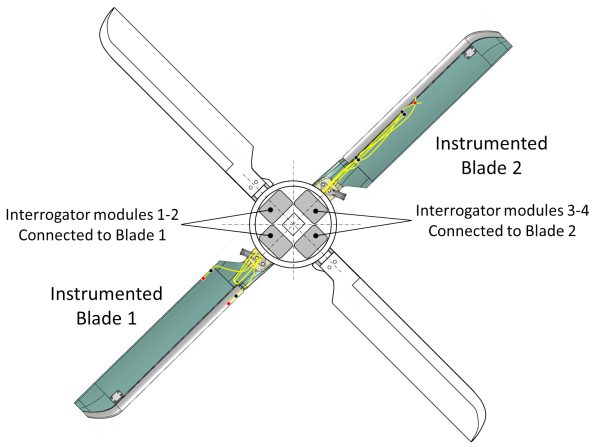

Figure 16: Scheme of tail rotor and the two instrumented blades

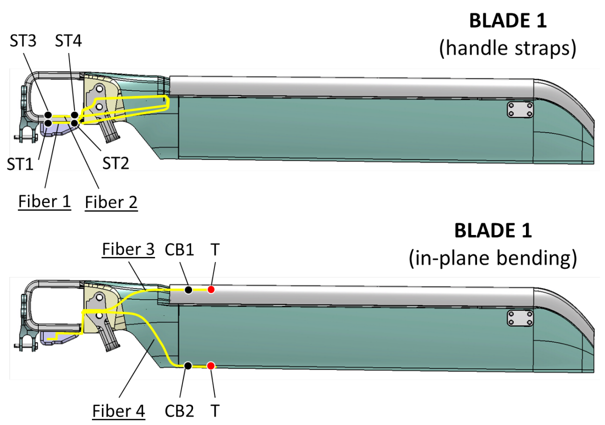

Figure 17: Scheme of FBG location on blade 1

Figure 16 illustrates how each of the two opposite instrumented blades is associated with a pair of interrogators, while Figures 17 and 18 show the location of the fibers and the FBGs on blade 1 and blade 2.

Figures 19 and 20 show some details of the blade root region derived from CAD studies which were aimed at optimizing the routing of the fibers within the blade structural layers.

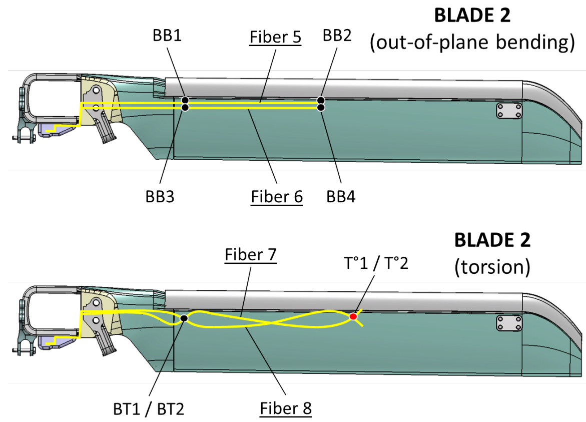

Figure 18: Scheme of FBG location on blade 2

Table 2: Fibers and sensors

Blade	Fiber	Sensor	WL	Load component
1	1	ST1	B	Strap axial (outer)
		ST2	R	Strap axial (outer)
	2	ST3	B	Strap axial (inner)
		ST4	R	Strap axial (inner)
	3	CB1	B	In-plane bending
		T	R	Temperature
	4	CB2	B	In-plane bending
		T	R	Temperature
2	5	BB1	B	Out-of-plane bending
		BB2	R	Out-of-plane bending
	6	BB3	B	Out-of-plane bending
		BB4	R	Out-of-plane bending
	7	BT1	B	Torsion
		T	R	Temperature
	8	BT2	B	Torsion
		T	R	Temperature

3.4. Fibers

Special fibers were adopted due to the specific application requirements. The need to minimize invasiveness in the laminates dictated the use of thin 80 μm diameter fibers[5], as is shown in the scheme of Figure 21. The fibers are single-mode with high numerical aperture and thus low sensitivity to bending, which is another practical feature for this implementation due to the need to accommodate tight bending radii. Furthermore they have an operating temperature exceeding 180 °C to sustain the curing cycles of the blade in autoclave. Finally the fiber coating is made of an organic ceramic material (ORMOCER) instead of the more common polyimide or polyacrylate. The new coating offers high adhesion to the fiber glass and high modulus to generate a good strain transfer between fiber and glue.

The fibers needed to be provided with a connec-

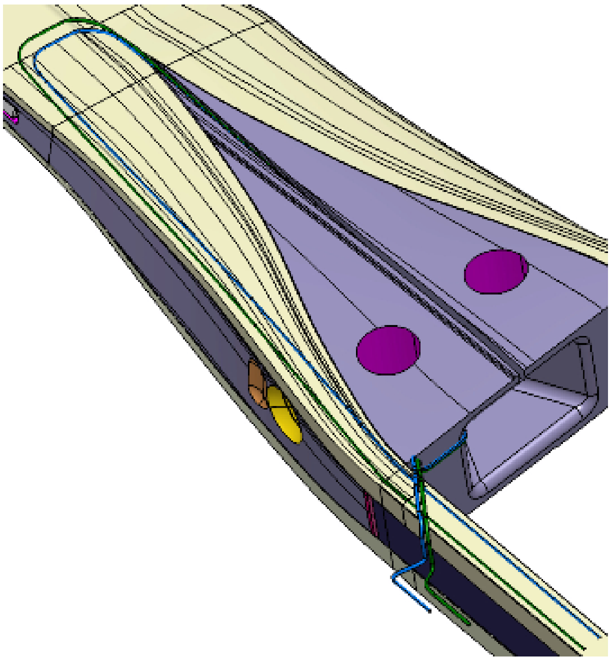

Figure 19: Blade 1 root region

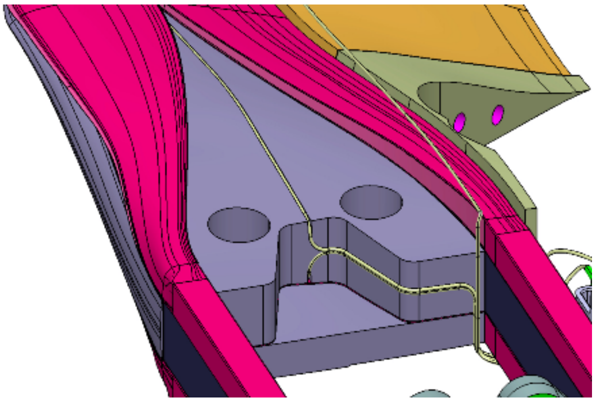

Figure 20: Blade 2 root region

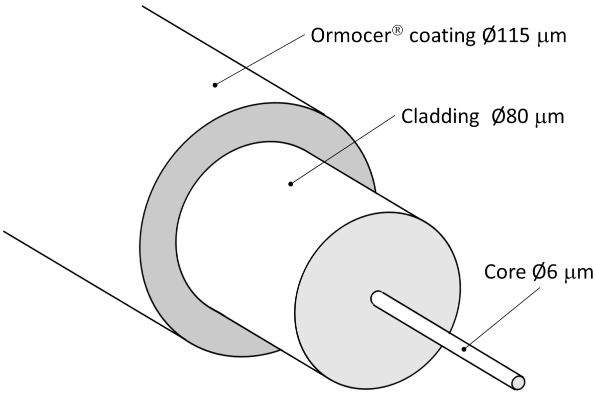

Figure 21: Fiber composition

tor prior to deposition on the laminate because it would have been impractical to perform the delicate connector installation on the field. Furthermore the connectors, like the fibers, needed to be temperature-resistant because they were exposed to blade curing.

The Mini-AVIM connector was therefore used due to its heat resistance and aerospace-grade specs. A PEEK protection tube extending to a certain fiber length from the connector (variable depending on the fiber location) was added as a protective sleeve, especially useful in the interface where the fiber exits from the laminate. A picture is shown in Figure 22.

Figure 22: A fiber FBG string with connector, shown inside its storage box. PEEK protective sleeve is visible in the first half coil

3.5. Thermal compensation

One of simplest methods available for temperature compensation consists in measuring the thermal strain through a dedicated FBG sensor used as a reference[6]. The reference FBG shall be located in the same thermal environment as the strain sensors and is encapsulated within a capillary and free to expand therein, thus becoming isolated from the structural strain field, as illustrated in Figure 23.

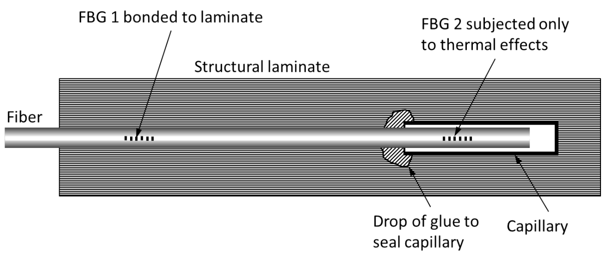

Figure 23: Scheme of the tenperature compensation system: FBG 2 is free to expand due to thermal effects and its strain can be subtracted from FBG 1

This approach was adopted for the blades; the temperature sensors indicated in Table 2 in-fact refer to FBGs encapsulated inside capillaries. Refer to the Appendix for an explanation of the rationale for thermal compensation.

3.6. Material Coupon Tests

Static and fatigue test campaigns were conducted to quantify the sensor system invasiveness and its potential impact on the mechanical behavior of the blade laminates[7]. A set of coupons was devoted to the assessment of the invasiveness of the capillary-based thermal compensation technique developed at Politecnico di Milano and on its effect on the mechanical behavior of the blade laminates. The test campaign was conducted on a set of both instrumented and non-instrumented specimens, the latter acting as a baseline for comparison. Three types of test coupons were built, representative of the following blade areas where the sensors are embedded:

- Strap in the blade handle region
- Trailing edge region
- Torque box in the blade spar

For each typology, two sets of specimens have been defined, one with the optical fiber incorporated and one blank to be used for reference. Each type of specimen consisted of 15 coupons subjected to a quasi-static test and four cycling load tests (with four different load levels defined as a percentage of the static strength value).

Figure 24 illustrates the static test up to failure of a specimen representative of the blade strap region. The qualitative behavior at varying levels of load was then compared for specimens with and without sensors.

The methods of damage propagation and ultimate failure were analyzed, verifying that the material coupons strength was not affected by the presence of the optical fiber or the capillary. As expected, the presence of optical fibers in the laminate does not translate in a detectable degradation of mechanical properties[8,9]; the invasiveness of the sensor is lower than the defects found in normal production, even when automated production techniques are used.

3.7. FBG Embedding Process

The laying of the fibers is hereafter described in detail for blade 2 (see Table 2) which was the first to be instrumented.

Figure 24: Ultimate static strength test on unidirectional strap coupon

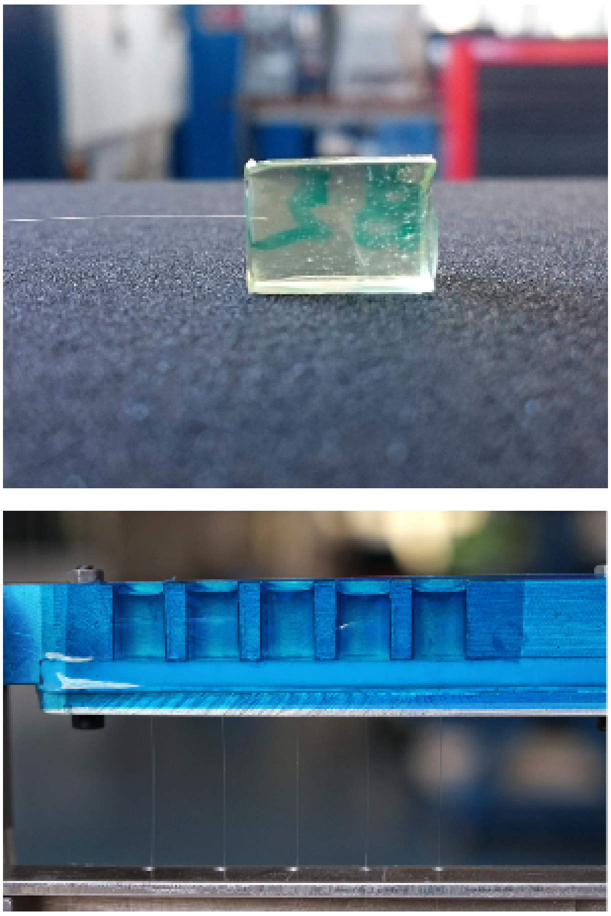

Figure 25: Top: fiber pull-out test coupon; bottom: pull-out experimental setup

The activities took place in Leonardo Helicopters' Anagni Center for Composites manufacturing, where rotor blades are fabricated. The production of the first experimental blade started with a batch of standard components, namely the upper and lower straps (unidirectional glass fiber composite), the integrated inner element and support block constituting the blade root and the Rohacell structural foam spar core.

Figure 26: The preliminary spar assembly before adhesive film application and torsion box fabrication

These are the elements which constitute the preliminary spar assembly, as shown in Figure 26.

The first step was represented by the construction of the spar; film adhesive was applied on straps, support block and core which were then bonded together. The item was then ready for FBG fiber laying (Figure 27).

The fibers had been prepared with their Mini-AVIM connector and PEEK protection tube covering a certain fiber length.

The first fibers to be installed were n. 5 and 6 (ref. Table 2) because these fibers are bonded directly on the UD straps for out-of-plane bending measurement.

The blade root support block had been machined to create upper and lower channel (to guide the fibers) and a cavity to enclose and protect the connectors during the curing cycles. Care was taken in laying fibers 5 and 6 in such a way that the sensors were placed at the right blade station. Special effort was made to ensure an adequate sealing between the fiber and the guiding groove to prevent resin from flowing inside and reaching the connector protection cavity during the spar curing cycle. In this phase, in-fact, the blade spar is placed in a mold under the action of pressure and temperature to allow resin to impregnate and bond the prepreg plies. Under these circumstances the resin flows with very low viscosity and can easily reach into the tiniest gaps.

A putty-like modelling clay was thus used as a sealing material, as illustrated in Figure 28. The naked fiber, where the two FBG sensors are located, was applied over the spar UD (uni-directional) fibers with a combination of adhesive film "stamps" and

Figure 27: The preliminary spar assembly after adhesive film application

the natural stickiness of the adhesive-covered spar surface. The perfect bonding of the fiber to the substrate would be guaranteed later, when the resin impregnates the fiber during the polymerization process. Figures 29 and 30 illustrate the spar after application of the upper and lower fibers for out-of-plane bending and the cavity used to protect the connectors during spar curing, machined inside the blade root block.

Having completed the deposition of fibers 5 and 6, it was time to resume work on the spar by applying the $\pm 45^\circ$ bidirectional plies which constitute the torsion box. There are multiple plies which are manually wrapper around the spar. This process is illustrated in Figure 31.

The fibers n. 7 and 8 were applied between plies to guarantee perfect integration inside the torsion box. These are in-fact the fibers which are designed to read torsion in the blade. For this reason the fiber portion with the FBG was positioned at 45°. The second FBG on fibers 7 and 8 is used for temperature monitoring and thus its orientation doesn't matter in principle because it is encapsulated in a capillary and free to expand therein.

Obviously, even these fibers' connectors had to be protected inside the root cavity. A difficulty to

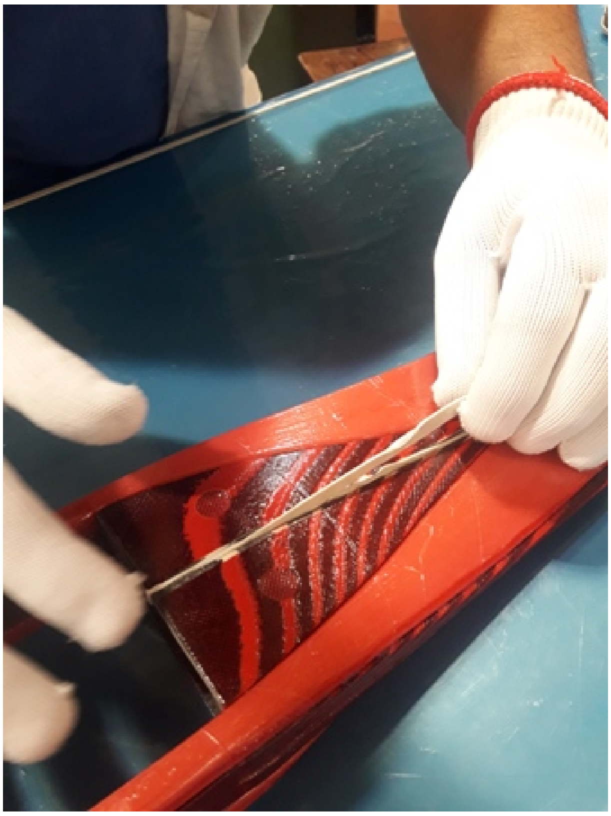

Figure 28: Sealing of the fiber guiding channel

Figure 29: The beam bending fibers after successful application to the spar top and bottom surfaces

overcome at this point was the fact that at this stage the spar was covered with bidirectional plies and thus the guiding groove was not accessible anymore as for the previous fiber pair.

Access to the cavity was therefore enabled by opening a small hole within the plies, but without braking fibers, rather by simply displacing them by just the amount necessary to allow passage for the fiber and its PEEK protection tube. This is illustrated in Figure 32.

During all phases the fibers were periodically interrogated with a portable source to ensure their integrity. The various steps are illustrated in Figure 32.

The capillary for temperature compensation is a metal tube of 0.1 mm diameter. Its invasiveness in the laminates had been verified through coupon testing and considered acceptable. Still, it represents a discontinuity of much larger proportions compared to the 0.0115 mm fiber it contains, see Figure 33. A smaller capillary tube could be foreseen in the future.

Obviously, also the capillary had to be sealed to avoid resin flowing inside and cementing the fiber. One end of the capillary had been sealed beforehand, while the other end had to be sealed on the spot with a tiny drop of glue to seal the gap between

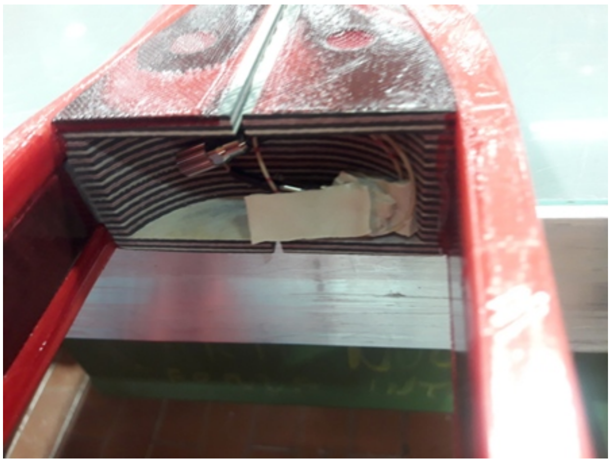

Figure 30: The receptacle for connector protection

fiber and tube.

Even the capillaries, and the FBG therein, were eventually oriented at 45 ° to make them parallel to one of the two fiber directions and thus minimize their protrusion and the defect within the ply.

At this point, with the four fibers laid down as shown in Figure 34, the four connectors were individually covered with protective Teflon coating and then packaged inside the root cavity, which was in-

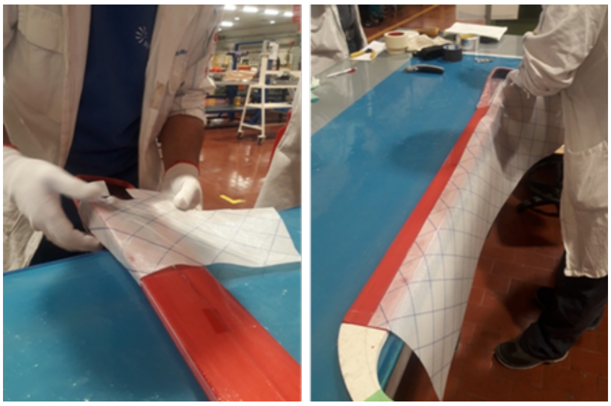

Figure 31: The spar being wrapped with bidirectional plies

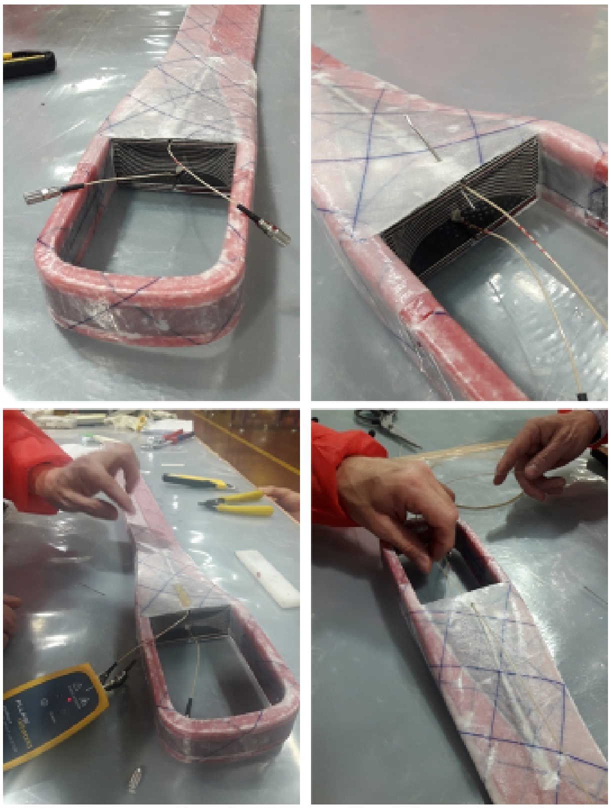

Figure 32: Clockwise from top left: the spar with the out-of-plane bending fibers, preparation of hole for the first torsion fiber, deposition of the first torsion fiber, checking fiber integrity

turn sealed from the outside with a protective cover to prevent resin flow (Figure 35).

The spar was then placed in the mold and cured under pressure.

The result was right first time, with very minor resin flow observed inside the cavity. The fibers' integrity was verified through interrogation.

The final manufacturing phase of the blade body

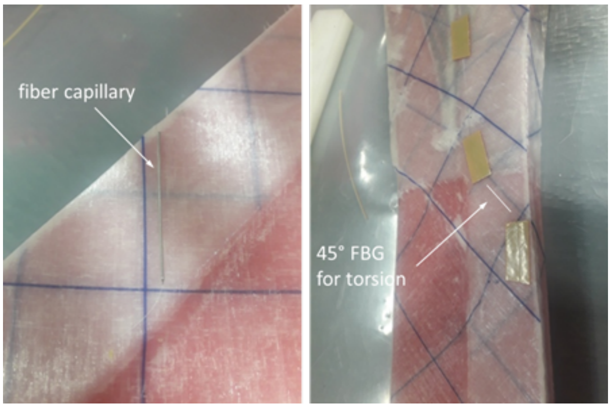

Figure 33: The 45 ° FBG for torsional strain and its temperature compensation capillary

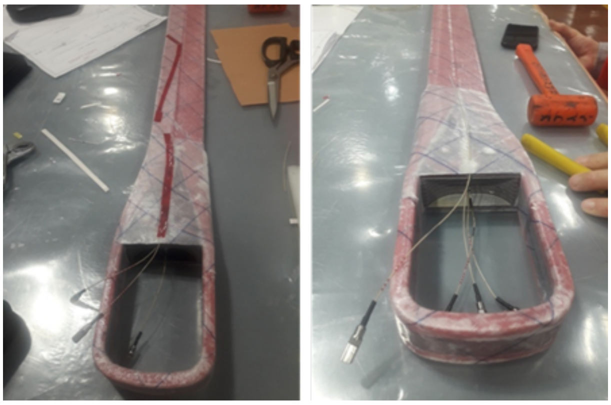

Figure 34: The third and fourth fibers of blade n. 2 successfully applied to the spar, with all the connectors exiting from the protection enclosure, prior to curing cycle

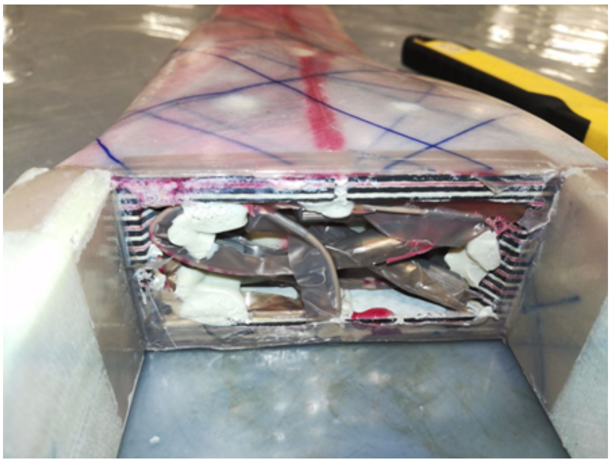

Figure 35: The teflon bags wrapped around the connectors successfully prevented resin contamination

involved a third polymerization cycle under pressure to bond the blade skins to the spar / rohacell trailing edge assembly. The fibers and connectors

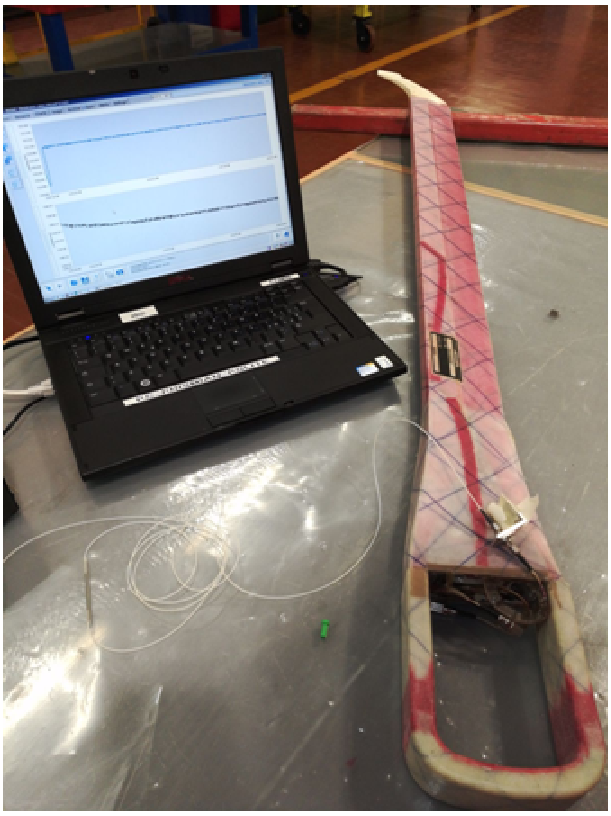

Figure 36: The fibers successfully tested after curing cycle of spar

survived the process with no damage. The semi-finished article is illustrated in Figure 37.

After deburring, additional steps involve the attachment of the mechanical fixtures for blade pitch link, damper connection and the elastomeric bearing.

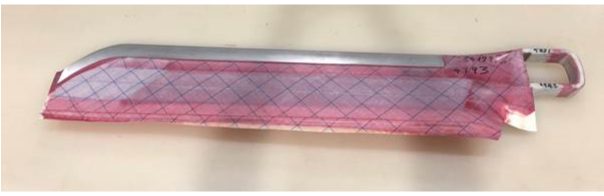

Figure 37: The blade body, complete with skin and erosion shield, just after being extracted from the mold. Note the excess resin which will require deburring and finishing.

Some conclusions can be derived from this first iteration. First we noted that some degree of flexibility and customization of processes was needed due to the difficulty in guaranteeing perfect alignment with drawings. It is preferable to start with fibers covered with PEEK tube on their full length and then strip them as needed because it is difficult to predict the exact path of the fiber.

4. CONCLUSIONS AND NEXT STEPS

We have presented an overview of the design, development and manufacturing of a tail rotor blade load monitoring system for the AW139 helicopter. Two of the four blades have been modified during their manufacturing process cycles by embedding fibers in a minimally invasive way. The FBG strain sensors in the fibers are interrogated by a custom-designed interrogation unit which was ruggedized for operation on a helicopter rotor.

A compact, lightweight and sturdy interrogator technology has been subjected to preliminary environmental qualification on a test bench. Furthermore the feasibility of embedding multiple optical fibers with high reliability and little impact on manufacturing was demonstrated.

The next step will consist in the integration of the instrumented beanie and the sensorized blades on the tail rotor rig illustrated in Figure 38 for full-scale rotor test.

Figure 38: The spin rig, a full scale AW139 tail boom with electric powered tail rotor

There are multiple benefits in this solution compared to legacy strain gages. First of all the FBG sensors are virtually immune to wear and tear due to their protected environment, this in turn allows operation in all weather conditions because sand and rain have no erosive effects on FBGs. Finally the lack of external sensors and cabling leaves a flush blade profile allowing higher speeds.

As the era of photonic integration on chip unfolds, we believe it is a worthy goal to pursue this technology with the objective of miniaturization of the interrogator. This could open the possibility of embedding the interrogation unit within the blade structure instead of having a separate installation on the beanie, thus avoiding the associated cabling, towards a self-contained instrumented blade unit.

REFERENCES

[1] A. Othonos and K. Kalli. *Fiber Bragg Gratings: Fundamentals and Applications in Telecommunications and Sensing*. Artech House Optoelectronics Library, 1999.

[2] L. G. Leka and E. Bayo. *A close look at the embedment of optical fibers into composite structures*. Journal of Composites, Technology and Research, Vol. 11, pp. 106-112, 1989.

[3] A. Wilson, S. W. James, and R. P. Tatam. *Time-division-multiplexed interrogation of fibre Bragg grating sensors using laser diodes*. Measurement Science and Technology, Vol. 12, pp. 181-187, 2001.

[4] W. Zhu, L. Qian, and A. S. Helmy. *Implementation of three functional devices using Erbium-doped Fibers: An Advanced Photonics Lab*. Department of Electrical and Computer Engineering, University of Toronto, 2007.

[5] K. Saton, K. Fukuki, Y. Kurosawa, A. Hongo, and N. Takeda. *Polyimide-Coated Small-Diameter Optical Fiber Sensors for Embedding in Composite Laminate Structures*. SPIE: Newport Beach, CA, USA, pp. 285-294, 2001.

[6] Z. Zhou and J. Ou. *Techniques of temperature compensation for FBG strain sensors used in long-term structural monitoring*. Proceeding of Asian Pacific Fundamental Problems of Opto- and Microelectronics (APCOM), 2004.

[7] D. W. Jensen and J.S. Sirkis. *Integrity of composite structures with embedded optical fibers. In Fiber Optic Smart Structures*. Udd, Eric, Ed.; Wiley, pp. 109-129, 1995.

[8] P. Bettini and G. Sala. *Preliminary assessment of helicopter rotor blades fatigue endurance through embedded f.o. sensors*. 24th ICAF Symposium, Naples, 2007.

[9] B.A. Sjogren. *Static strength of CFRP laminates with embedded fiber-optic edge connectors*. Composites Part A: Applied Science and Manufacturing, Vol. 32, pp. 189-196, 2001.

[10] M.H. Song, S.B. Lee, S.S. Choi, and B.H. Lee. *Simultaneous measurement of temperature and strain using two fiber Bragg gratings embedded in a glass tube*. Optical Fiber Technology, Vol. 3, 194-196, 1997.

[11] N. Tanaka, Y. Okabe, and N. Takeda. *Temperature-compensated strain measurement using fiber Bragg grating sensors embedded in composite laminates*. Smart Structures and Materials, Society of Photo-Optical Instrumentation Engineers (SPIE), Vol. 4694, 2002.

A. APPENDIX

A.1. FBG Thermal Compensation

FBG sensing is based on the Bragg grating ability to reflect a specific spectral component of the incident light, this component being linked to the grating periodicity (Λ) and its effective refractive index (n_{eff}). The grating behaves therefore as a sort of semi-reflective mirror.

The peak wavelength shift of the reflected spectrum compared to a nominal value (λ_B) represents the cumulative effect of the factors which have perturbed the Bragg grating periodicity, its effective refractive index or both. One of these factors is mechanical strain, the other is temperature.

If one is able to decouple the effect of temperature, then the mechanical strain in the fiber can be derived[10 11].

The basic relation linking the reflected peak wavelength to the FBG characteristics is given by:

(1) $$\lambda_B = 2n_{eff}\Lambda$$

By differentiation we obtain

(2) $$d\lambda_B = 2\Lambda dn_{eff} + 2n_{eff}d\Lambda$$

Dividing (2) by (1) we obtain

(3) $$\frac{d\lambda_B}{\lambda_B} = \frac{dn_{eff}}{n_{eff}} + \frac{d\Lambda}{\Lambda}$$

In the above equation $\frac{d\Lambda}{\Lambda} = \epsilon$ represents the mechanical strain. The effective index n_{eff} is affected by strain as shown by the relation

(4) $$\frac{dn_{eff}}{n_{eff}} = -\frac{n_{eff}^2}{2}[p_{12} - \nu(p_{11} + p_{12})]\epsilon$$

Where p_{11}, p_{12} are the elasto-optic coefficients and

(5) $$P = \frac{n_{eff}^2}{2}[p_{12} - \nu(p_{11} + p_{12})]$$

is the photoelastic constant of the material, depending from Poisson's ratio of glass ν, see Figure 39 for the fiber reference system. The relation then becomes

(6) $$\frac{d\lambda_B}{\lambda_B} = \epsilon(1 - P)$$

Assuming a wavelength $\lambda_B = 1550\ nm$ and realistic value of P for the glass of a fiber (silicon dioxide) of 0.22, this translates in a strain sensitivity of 1.21 $pm/\mu\epsilon$

When thermal effects are considered, we observe that temperature has a double role: it causes an

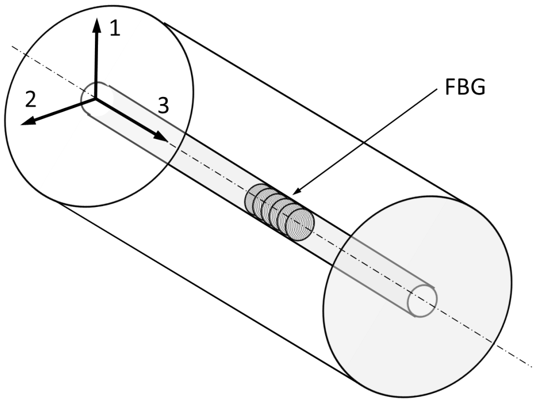

Figure 39: The fiber reference system

elongation of the FBG and thus alters its periodicity Λ, but also changes the refractive index n_{eff}; the combined thermal effect is obtained differentiating (1) by temperature

(7) $$d\lambda_B = 2(\Lambda \frac{dn_{eff}}{dT} + n_{eff}\frac{d\Lambda}{dT})dT$$

again, dividing by (1) we obtain

(8) $$\frac{d\lambda_B}{\lambda_B} = (\frac{1}{n_{eff}}\frac{dn_{eff}}{dT} + \frac{1}{\Lambda}\frac{d\Lambda}{dT})dT$$

which can be written as

(9) $$\frac{d\lambda_B}{\lambda_B} = (\zeta + \alpha)dT$$

The quantities $\zeta = \frac{1}{n_{eff}}\frac{dn_{eff}}{dT}$ and $\alpha = \frac{1}{\Lambda}\frac{d\Lambda}{dT}$ represent the thermo-optical and thermal expansion coefficients respectively.

To put things in perspective, $\alpha = 0.55x10^{-6}K^{-1}$ for silica glass, while ζ values can range between $3.0x10^{-6}K^{-1}$ and $8.0x10^{-6}K^{-1}$, therefore the effect on the refractive index is much bigger than the thermal expansion.

The resulting temperature sensitivity coefficient for a wavelength $\lambda_B = 1550\ nm$ is in the order of 10 pm/K.

Considering that aeronautical operational conditions typical range between $-50°C$ and $+40°C$, this means that an FBG wavelength variation of up to a $900pm$ can result due to environmental conditions alone, which corresponds to a strain of over $740\mu\epsilon$.

Obviously such a significant value cannot be ignored in a strain measurement system which is expected to measure in a range of a few thousand $\mu\epsilon$, as is the case here described.

The capillary based system implemented on the blades, described in this work, allows filtering out the thermal effects from the FBG strain readings.